Wetting hysteresis of nanodrops on nanorough surfaces

Cheng-Chung Chang,[1] Yu-Jane Sheng,[1,*] and Heng-Kwong Tsao[2,†]
[1]*Department of Chemical Engineering, National Taiwan University, Taipei 106, Taiwan*
[2]*Department of Chemical and Materials Engineering, National Central University, Jhongli 320, Taiwan*
(Received 22 July 2016; published 24 October 2016)

Nanodrops on smooth or patterned rough surfaces are explored by many-body dissipative particle dynamics to demonstrate the influence of surface roughness on droplet wetting. On a smooth surface, nanodrops exhibit the random motion and contact angle hysteresis is absent. The diffusivity decays as the intrinsic contact angle (θ_Y) decreases. On a rough surface, the contact line is pinned and the most stable contact angle (θ'_Y) is acquired. The extent of contact angle hysteresis ($\Delta\theta$) is determined by two approaches, which resemble the inflation-deflation method and inclined plane method for experiments. The hysteresis loop is acquired and both approaches yield consistent results. The influences of wettability and surface roughness on θ'_Y and $\Delta\theta$ are examined. θ'_Y deviates from that estimated by the Wenzel or Cassie-Baxter models. This consequence can be explained by the extent of impregnation, which varies with the groove position and wettability. Moreover, contact angle hysteresis depends more on the groove width than the depth.

DOI: 10.1103/PhysRevE.94.042807

I. INTRODUCTION

The wetting of a solid surface by a liquid is ubiquitous in everyday life and industrial applications, such as cleaning, printing, and microfluidics. The wettability is generally expressed in terms of the contact angle (CA) between liquid-gas and solid-liquid interfaces. On a smooth surface, the intrinsic CA (θ_Y) depends on the chemical composition only and is described by Young's equation [1],

$$\cos\theta_Y = \frac{\gamma_{sg} - \gamma_{sl}}{\gamma_{lg}}, \tag{1}$$

where γ_{ij} is the interfacial tension between i and j phases. The subscripts g,l, and s represent gas, liquid, and solid, respectively. When the CA is less than 90°, the surface is generally referred to as being lyophilic. On the contrary (CA greater than 90°), it is lyophobic. However, ideal surfaces rarely exist in nature and surface roughness always occurs on real surfaces. It is believed that the wetting behavior is considerably influenced by surface roughness as well [2–6]. Typically, two theoretical models are widely employed to explain how surface roughness affects the CA. For the completely wetted rough surface, the apparent CA (θ) is related to θ_Y by the Wenzel model [7]

$$\cos\theta = r\cos\theta_Y, \tag{2}$$

where r is the area ratio of the wetted surface to the projected one ($r \geqslant 1$). Due to the increment of the solid-liquid contact area, surface roughness amplifies the lyophilicity for lyophilic surfaces but raises the lyophobicity for lyophobic surfaces. On the other hand, for the completely nonwetted rough surface with the air pockets, θ can be determined by the Cassie-Baxter model [7]

$$\cos\theta = \alpha\cos\theta_Y + (1-\alpha)\cos(180^\circ). \tag{3}$$

where α represents the area fraction of the wetted surface ($\alpha < 1$). The air pockets with the CA 180° always enhance surface lyophobicity ($\theta > \theta_Y$).

The above theories imply a unique CA for a liquid on a surface. In fact, the CA is always in a range bounded by θ_a and θ_r on a surface, where θ_a and θ_r represent the advancing and receding CAs, respectively. Upon the inflation and deflation of the drop, it is observed that the contact line is pinned for $\theta_r \leqslant \theta \leqslant \theta_a$. For the outward or inward movement of the contact line, the CA should achieve θ_a or θ_r first, respectively. The difference between θ_a and θ_r is defined as the extent of contact angle hysteresis (CAH), $\Delta\theta = \theta_a - \theta_r$. Three mechanisms are generally invoked to explain the existence of CAH: pinning by chemical defects [3,8,9], adhesion hysteresis [9–12], and surface roughness [6,13–15]. In the first mechanism, the contact line is mechanically trapped by the lyophilic defects upon retraction. The extent of CAH is strongly affected by the size and lyophilicity of the blemishes. In the second mechanism, the restructuring of the solid surface such as polymerlike materials is induced by the liquid-solid contact to reduce the system energy. As a result, the solid-liquid interfacial tension is lowered from γ_{sl} associated with θ_a to γ'_{sl} associated with θ_r [10]. In the third mechanism, surface grooves lead to a series of stable drop shapes with different apparent CAs [6,14]. Typically, periodic surfaces are used to demonstrate these metastable states separated by the energy barrier, which cannot be overcome by thermal fluctuations. Note that for the cases of random surfaces with small roughness, this mechanism coincides with the first mechanism [3,16].

Recently, the advance of science and technology has promoted the miniaturization, leading to the structures on the nanoscale eventually. For example, the structures in semiconductor manufacturing are shrunk to be nanoscaled to achieve higher performance. As a result, the exploration of the wetting phenomena on the microscale, or even nanoscale becomes important for the further developments in nanotechnology [17–21]. CAH is essential in understanding of the wetting mechanism and CAH of nanodrops on substrates can be investigated by simulations [22–29]. Unfortunately, very few works are reported in the literature. Nanodrops on randomly rough surfaces has been explored by molecular dynamics [24]. It is shown that on hydrophobic surfaces, nanodrops are in the Cassie-Baxter state and CAH is absent. On hydrophilic surfaces, in contrast, strong CAH is observed.

*yjsheng@ntu.edu.tw
†hktsao@cc.ncu.edu.tw

In addition, CAH of a drop on lyophobic patterned surfaces (pillar and grid) immersed in an immiscible liquid has been studied by dissipative particle dynamics (DPD) [23]. While CAH is insignificant on the homogeneous substrate or at high temperature, it becomes substantial on patterned surfaces at low temperature. Contact line motion can also be simulated by the Lattice-Bolztmann technique, which is a mesoscale approach [30–32].

The wetting phenomena for microdrops or larger drops on rough substrates have been widely investigated both experimentally and theoretically. As the drop size and surface roughness get down to the nanoscale, however, the validity of Young's equation is controversial because of the effect of the line tension [33]. The applicability of the Wenzel or Cassie-Baxter model becomes questionable [26–28,34,35]. Moreover, how the nanoscale roughness alters the extent of CAH is still unknown. The pinning of the contact line, which always occurs in microscale experiments is not observed in simulations of nanodrops [23,24]. In this work, the wetting behavior of a nanodrop sitting on a rough surface in equilibrium with its vapor is explored by many-body dissipative particle dynamics (MDPD), which is able to simulate a drop-vapor system [36]. In Sec. II, MDPD simulation methodology is briefly introduced. The calculation of the interfacial tensions and the determination of the CA for nanodrops are also presented. In Sec. III A, the validity of Young's equation is examined by considering a nanodrop on the smooth surfaces with various wettabilities. In Sec. III B, the CAH loop, which always exists in microscale experiments, is acquired by the inflation-deflation method in our simulations. θ_a and θ_r are also determined by the inclined plane method. The consistency between these two methods is studied. In Secs. III C and III D, by studying various patterned rough surfaces, the influences of surface roughness and wettability on CAH are demonstrated. Finally, conclusions of this work are included in Sec. IV.

II. SIMULATION METHOD

A. MDPD simulations

MDPD is modified from classical DPD to simulate a gas-liquid system [36]. In MDPD, the conservative force f_{ij}^C consists of both attractive and repulsive potentials,

$$f_{ij}^C = a_{ij}\omega_c(r_{ij})\mathbf{e}_{ij} + b_{ij}(\overline{\rho}_i + \overline{\rho}_j)\omega_d(r_{ij})\mathbf{e}_{ij}, \qquad (4)$$

where $a_{ij} < 0$ and $b_{ij} > 0$ are the attractive and repulsive parameters between two particles i and j, respectively. $r_{ij} = |\mathbf{r}_{ij}|$ is the distance between the positions of particles i and j and $\mathbf{e}_{ij} = \mathbf{r}_{ij}/r_{ij}$ is the direction vector. The weight functions are chosen as $\omega_c(r_{ij}) = 1 - r_{ij}/r_c$ and $\omega_d(r_{ij}) = 1 - r_{ij}/r_d$. They decline linearly with interparticle separation and vanish as $r_{ij} \geqslant r_c$ for $\omega_c(r_{ij})$ and as $r_{ij} \geqslant r_d$ for $\omega_d(r_{ij})$. In this work, $r_c = 1.0$ and $r_d = 0.75$ are set. The amplitude of the repulsions depends on the local density $\overline{\rho}_i$ and $\overline{\rho}_j$. The random and dissipative forces are the same as those in DPD [37,38].

The dimensionless form is used and all the units are scaled by particle mass m, cutoff radius r_c, and thermal energy k_BT. The parameters used in this work are selected according to Warren's work [36] and listed in Table I. Generally, $a_{ij} = -40$ and $b_{ij} = 25$ are set. For the sake of generality, no specific test liquids and solid surfaces are considered. The liquid can be oil or water. As a result, a_{ij} between solid and liquid beads is varied to obtain different wettability, which depends only on the interfacial tensions on a smooth surface according to Young's equation. The difference of interactions between liquid-liquid beads and solid-liquid beads comes mainly from the attractive coefficient (a_{ij}). The former is $a_{ll} = -40$ while the latter is $a_{sl} = (-40) \sim (-15)$. The simulation system is a cubic box (90^3). The lower boundary is a solid substrate with varying wettability while the upper boundary is a wall with very low wettability. The x and y directions are subjected to the periodic boundary conditions. The number densities of liquid and solid beads are 6 and 8, respectively. The total number of MDPD liquid beads varies from 1.4×10^5 to 2.3×10^5. At least 5×10^5 steps are run for each simulation and the first 2.5×10^5 steps are for equilibration.

TABLE I. Parameters in the MDPD scheme (in MDPD units).

Name of parameter	Symbol of parameter	Value
Attractive coefficient	a_{ij}	$(-40) \sim (-15)$
Repulsive coefficient	b_{ij}	25
Time step	Δt	0.01
System temperature	k_BT	1.0
Random coefficient	σ	3.0
Dissipative coefficient	γ	4.5
Empirical velocity	λ	0.65
Verlet coefficient		

B. Surface tension calculations

In our simulations, interfacial tensions γ_{12} between phases 1 and 2 are computed according to Irving-Kirkwood expression [39,40]

$$\gamma_{12} = \int \{P_{zz}(z) - [P_{xx}(z) + P_{yy}(z)]/2\}dz, \qquad (5)$$

where P_{xx}, P_{yy}, and P_{zz} are the components of the pressure tensor with the coordinates x, y, and z. The components are defined as

$$P_{\alpha\alpha}(\alpha = x,y,z) = \rho k_BT + \frac{1}{V}\left[\sum_{i>j}\sum_{j}(r_{ij})_\alpha\left(f_{ij}^C\right)_\alpha\right], \qquad (6)$$

where ρ is the number density and V the system volume. $(r_{ij})_\alpha$ and $(f_{ij}^C)_\alpha$ denote the α component of r_{ij} and f_{ij}^C, respectively. The first term is the kinetic energy contribution from the particle momentum and the second term comes from interaction potential energy contribution. After the values of each pressure component become essentially constant over a sufficiently long period, the interfacial tensions are calculated. For the set of parameter above, $\gamma_{sg} = 14.3$ and $\gamma_{lg} = 7.5$ are obtained. In the simulation for surface tension calculation, a thick liquid layer is formed in the system and the effect of capillary waves on the liquid-vapor interface is eliminated by enough sampling.

C. Contact angle determination

After the system equilibrium is reached, simulation snapshots are acquired every 1×10^4 steps for total 5×10^4

steps. For each snapshot, CA for a nanodrop on a surface is then obtained by using the software provided by the CA goniometer, OCA 15EC (Data Physics, Germany). If the size of a DPD bead is about 10 nm, then the droplet size is about 500 nm. Such a calculation is not feasible for conventional molecular dynamics. The ellipse fitting mode, which uses the complete drop shape for the CA measurement is selected. First, the liquid-gas and solid-liquid interfaces of the nanodrop are determined manually. The smooth fitting curves are then provided by the software. After the CA of each snapshot is acquired, the mean value of the CA is calculated. The standard deviation of the CA is less than 2.5°.

III. RESULTS AND DISCUSSION

The simulation outcomes for the wetting behaviors of nanodrops on smooth or patterned rough surfaces are presented. Both lyophilic and lyophobic substrates are considered. On smooth surfaces, the values of the interfacial tension are calculated via Irving-Kirkwood equation. The CA obtained from Young's equation is compared to that determined directly from MDPD. Whether a nanodrop is pinned on a smooth surface or not is examined by following its trajectory due to thermal fluctuations. On patterned rough surfaces, CAH exists and its extent is decided by two typical techniques employed in macroscopic experiments. The comparison between outcomes from these two approaches are made. According to our simulation outcomes, the mechanism of CAH resulting from surface roughness is explained.

A. Nanodrops on a smooth surface

First of all, a smooth surface without nanoscaled roughness is considered and its solid-gas tension is $\gamma_{sg} = 14.3$. A nanodrop with surface tension $\gamma_{lg} = 7.5$ is deposited on the surface. The equilibrium shape of a drop varies with the attractive parameter ($a_{sl} < 0$) between solid and liquid particles. The values of the solid-liquid tension ($\gamma_{sl} > 0$) calculated by Eq. (5) via MDPD simulations and CAs evaluated by Young's equation (θ_Y) are listed in Fig. 1(a). As $|a_{sl}|$ is increased, solid beads like liquid ones more, γ_{sl} declines, and θ_Y decreases accordingly. As shown in the side view of the drop, the base

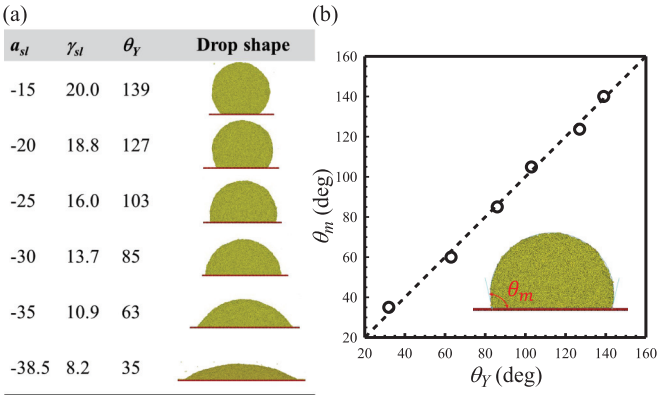

FIG. 1. (a) The variation of surface tension, CA evaluated by Young's equation, and drop shape with solid-liquid attractive parameter. (b) The comparison between CAs determined by Young's equation (θ_Y) and obtained by simulations (θ_m).

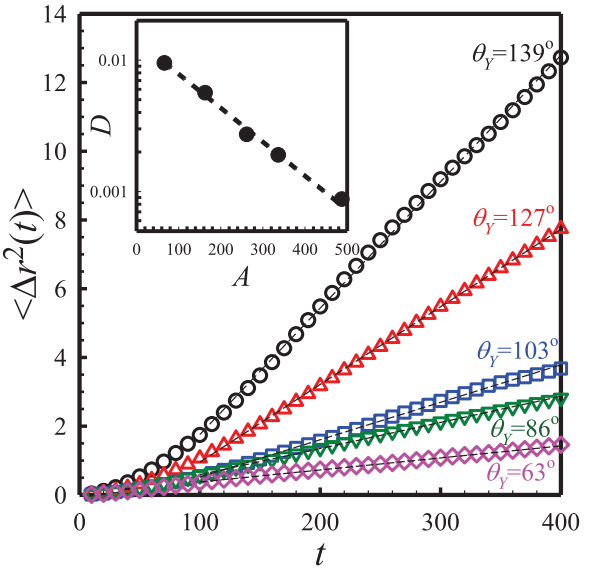

FIG. 2. The mean-squared displacement $\langle \Delta r^2(t) \rangle$ is plotted against the time t for nanodrops with different θ_Y. The inset shows the variation of the diffusion coefficient D with the contact area A.

diameter of the solid-liquid contact area grows and the CA is getting smaller. Note that the volumes of all droplets shown in Fig. 1(a) are the same. According to the Kelvin equation, the vapor pressure should vary with the radius of curvature. To examine the validity of Young's equation, CAs obtained directly from simulations (θ_m) are compared to the theoretical value θ_Y. The values of θ_m agree quite well with those of θ_Y and a linear line with the slope of +1 is clearly seen in the θ_Y-θ_m plot of Fig. 1(b). The maximum difference between θ_Y and θ_m is no more than 3°. Consequently, Young's equation is valid for nanodrops in our simulations and thus the contribution of the line tension is negligible.

Unlike a macroscopic drop, a nanodrop on a smooth surface exhibits the two-dimensional random motion due to significant thermal fluctuations. Figure 2 shows the mean-squared displacement $\langle \Delta r^2(t) \rangle$ for a drop with volume 2083, where $r(t)$ is the position of the center of mass of the drop from the origin at the time t. For sufficiently long time, e.g., $t > 100, \langle \Delta r^2(t) \rangle$ is proportional to t. That is, the nanodrop displays the Brownian motion described by

$$\langle \Delta r^2(t) \rangle = 4Dt, \tag{7}$$

where D represents the diffusion coefficient of the sessile nanodrop and can be estimated from the slope of the linear line in Fig. 2. It is found that D grows with θ_Y or it descends with the base diameter. The diffusion coefficient is plotted against the contact area A in the inset of Fig. 2. Apparently, D decays exponentially with the increase in A. As a result, when a drop is large enough, thermal fluctuations are unable to drive its random motion. The Brownian motion of a nanodrop also reveals the absence of contact line pinning or CAH on a smooth surface.

B. CAH determined by two methods used in experiments

On a smooth surface, a nanodrop exhibits the random walk and CAH is absent. However, as grooves are present

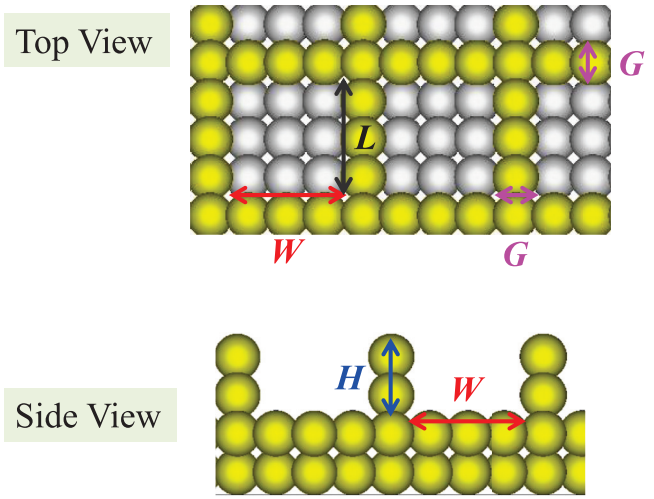

FIG. 3. The structure of the patterned rough surface with cuboidal cavities. L,W, and H represent the length, width, and depth of the groove, respectively. G is the distance between two adjacent cavities.

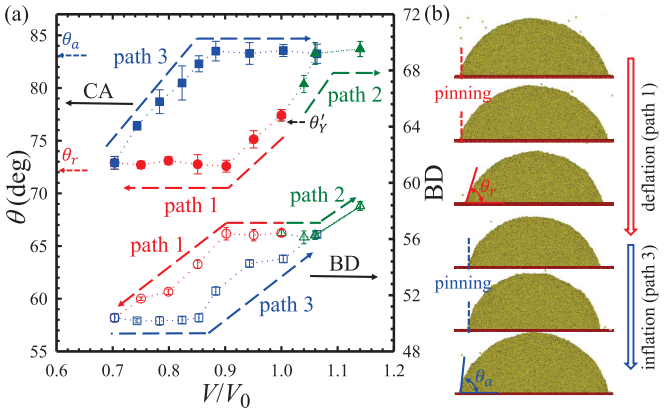

FIG. 4. (a) The variation of the apparent CA (θ) (top loop) and base diameter of the drop (BD) (bottom loop) with the drop volume (V). (b) Some snapshots associated with the hysteresis loop.

on the surface, its random motion is inhibited, indicating the appearance of CAH. In this work, a patterned rough surface is created with cuboidal cavities, as shown in Fig. 3. The substrate consists of four layers and the beads of the substrate are arranged in simple cubic structure. The cavity is a square mesh and its length, width, and depth are $L = 1.5, W = 1.5$, and $H = 1.0$, respectively. The distance between two adjacent cavities is $G = 0.5$. The extent of CAH is generally determined by two approaches in macroscopic experiments: the inflation-deflation and inclined plane methods. Therefore, they are adopted in our simulations to explore the extent of CAH for a nanodrop on the patterned rough surface. Although the CA on the smooth surface is unique, $\theta_Y = 85°$, the CA on a rough surface is distributed in a range and dependent on its history. When a spherical nanodrop is deposited on the patterned rough surface, the equilibrium CA is reduced to $\theta'_Y \approx 77°$. Typically, θ'_Y is referred to as the most stable CA, which will be explained later in the determination of CAH by the inclined plane method. It is essentially independent of the location on the surface and the drop size.

This result agrees reasonably with the prediction of the Wenzel model based on the area ratio $r \approx 2.5, \theta'_Y \approx 78°$. The typical hysteresis loops for the apparent CA (θ) and base diameter of the drop (BD) are acquired and demonstrated in Fig. 4(a) by employing the inflation-deflation method in which a group of particles are directly added or removed from the top of the drop and then the system will evolve toward equilibrium. For the sessile drop of initial volume $V_0 = 3.33 \times 10^4$, the CA declines but its BD remains unchanged as a small portion of liquid is removed from the drop stepwise (path 1). If the drop volume (V) continues decreasing, the CA reaches a lower bound, $\theta_r \approx 72°$. Afterwards, the contact line starts to move inward but the CA stays at $\theta \approx \theta_r$. In contrast, upon the addition of liquid to the drop with V_0, the CA rises from θ'_Y with constant BD (path 2). Eventually, the CA arrives at an upper bound, $\theta_a \approx 83°$. Subsequently, the contact line starts to move outward but the CA stays at $\theta \approx \theta_a$. The direct growth from θ_r to θ_a accompanied with a pinned contact line can be achieved by inflating a shrunk drop (path 3). Note that the variation of BD tends to be steplike due to the periodical roughness. Some snapshots for a nanodrop on the patterned rough surface during inflation and deflation are depicted in Fig. 4(b).

In the inclined plane method, a horizontal external force is exerted on the nanodrop to mimic the horizontal component of gravitational force in macroscopic experiments. The vertical force can be neglected for small Bond numbers, which are defined as the ratio of gravitational force to surface tension force. Figure 5(a) depicts the variation of the drop shape with the applied force (f) for a drop volume 3.33×10^4. As f is increased, both the frontmost and rearmost contact lines stay pinned due to surface roughness. Therefore, the front CA grows and the rear one declines with increasing f. As f exceeds a critical value (f_c), the pinning force induced by roughness is overcome and the drop starts to move. The front CA (θ_f), rear CA (θ_b), and major length (l_m) are shown in Fig. 5(b). The major length is defined as the length between the rightmost and leftmost sides of the drop along the direction of the external force. The major length does not vary with f,$l_m \approx 56.4$, because of the contact line pinning. Simultaneously, θ_f grows toward the advancing CA while θ_b

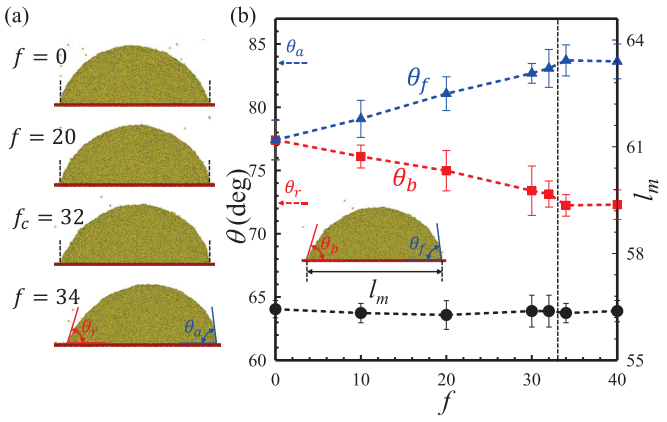

FIG. 5. (a) The variation of the drop shape with the applied force (f). (b) The plot of the front CA (θ_f), rear CA (θ_b), and major length (l_m) against f.

TABLE II. Simulation outcomes for the nanodrop on the rough surfaces of various wettability (θ_Y). The patterned roughness is specified as $L = W = 1.5, H = 1.0$, and $G = 0.5$.

θ_Y	θ'_Y	BD	$\Delta\theta$	f_c	n_a
127	141	28	0	0	1.5
113	124	35	3.6	3	4.9
103	112	40	8.0	12	7.4
85	77	56	11.1	32	9.5
76	59	64	5.2	16	10.1
63	43	72	–	–	11.0

declines toward the receding CA. Eventually, one observes $\theta_f = \theta_a$ and $\theta_b = \theta_r$ as $f \simeq f_c = 32$. When f exceeds f_c, the frontmost and rearmost contact lines start to move forward at the same time. The foregoing wetting behaviors agree qualitatively with those reported in experiments for the most stable CA [41–43]. Consequently, the initial condition in our simulations (the spontaneous partial wetting of a spherical drop) yields θ'_Y corresponding to the most stable CA. Note that both θ_a and θ_r determined from the inclined plane method are the same as those from the inflation-deflation method. This consequence reveals that both approaches are valid in simulations for exploring CAH of a drop on a rough surface. For convenience, the inclined plane method is used in the following.

C. Effect of wettability on the most stable CA and CAH

Although the hysteresis-free behavior is shown on the smooth surface with $\theta_Y = 85°$, contact line pinning with $\Delta\theta = \theta_a - \theta_r \approx 11°$ is clearly observed by the inclined plane method as the surface becomes rough. Under a specified patterned roughness ($L = W = 1.5, H = 1.0$, and $G = 0.5$), CAH is anticipated to change if the wettability of liquid on solid surface (θ_Y) is varied. The simulation outcomes are listed in Table II for various values of θ_Y. Note that the wettability can be changed by altering the attractive coefficient (a_{ij}) in Table I. As the wettability is increased, the most stable CA (θ'_Y) declines but the base diameter (BD) grows monotonically. On lyophobic surfaces ($\theta_Y > 90°$), θ'_Y is evidently greater than θ_Y due to lyophobic grooves or air pockets. This fact is qualitatively consistent with the Wenzel and Cassie-Baxter models. However, both models overestimate θ'_Y. The prediction of the Cassie-Baxter model (area fraction $\alpha = 0.44$) is closer to the simulation value for $\theta_Y = 113°$ and $127°$ while that of the Wenzel model (area ratio $r = 2.5$) is closer for $\theta_Y = 103°$. On lyophilic surfaces ($\theta_Y < 90°$), θ'_Y is obviously less than θ_Y because of the impregnation of lyophilic grooves. While the Wenzel model describes θ'_Y of the rough surface with $\theta_Y = 85°$ well, it underestimates θ'_Y for $\theta_Y = 76°$ and predicts the total wetting behavior ($\theta'_Y \approx 0°$) for the rough surface with $\theta_Y = 63°$.

The discrepancy between the theoretical models and our simulation results can be realized by the impregnation of patterned grooves. Figure 6(a) shows the side view slice of the sessile nanodrop on the rough surface with various θ_Y. It seems that the impregnation is generally inevitable and only the lyophobic surface with $\theta_Y = 127°$ is slightly impregnated. The extent of the impregnation is further illustrated in the contour plot of liquid beads in grooves, as shown in Fig. 6(b). The maximum capacity of liquid beads within a groove can be theoretically evaluated by the product of liquid density (6) and the groove volume (2.25) and it is about 13.5. As expected, the extent of impregnation in terms of average amount of liquid beads per groove (n_a) decreases with increasing θ_Y. On a specific surface, however, there is a nonuniform distribution of liquid in grooves. Some grooves have more liquid than others. In general, the grooves near the edge of the drop contain less liquid than those in the center. According to these results, one can conclude that the effective area ratio (r) in the Wenzel model and the effective area fraction (α) in the Cassie-Baxter model are smaller than their intrinsic values. This explains why the overestimation of theoretical models for lyophobic surfaces and underestimation for lyophilic surfaces. While the Wenzel model can qualitatively describe our MDPD results on lyophilic rough surfaces, it fails to depict some results of density functional theory calculations and molecular dynamics simulations. In the latter, the increment of CA due to surface roughness is attributed to the contribution of the line tension or the incomplete impregnation of lyophilic grooves [26–28,34].

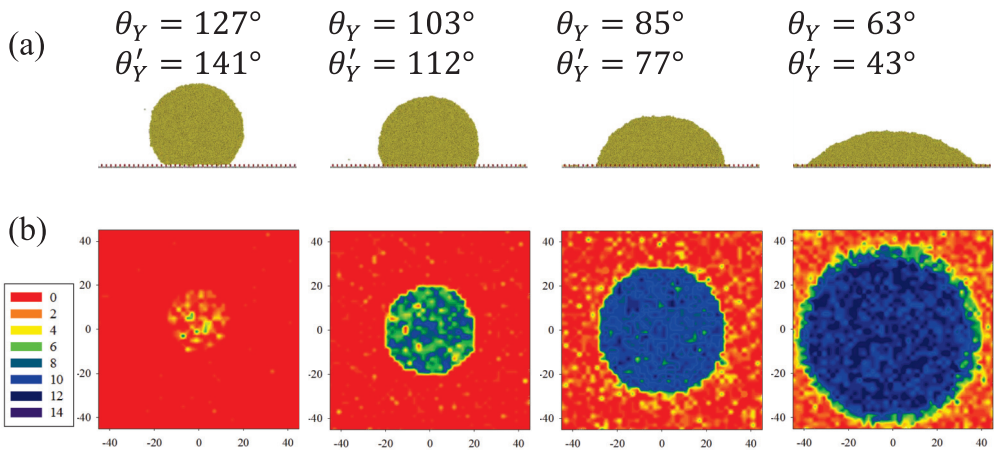

FIG. 6. (a) The side view slice of the sessile nanodrop on the patterned rough surfaces with various θ'_Y. (b) The extent of impregnation is exhibited by the contour plot of liquid beads in grooves with various θ'_Y.

TABLE III. Simulation outcomes for the nanodrop on the rough surfaces of $\theta_Y = 85^\circ$. The structure of roughness (W or H) is systematically varied.

W	H	r	S_a	θ'_Y	$\Delta\theta$	f_c	n_a
1.5	0.5	1.75	0.25	81	3.9	8	4.5
1.5	1.0	2.50	0.49	77	11.1	32	9.5
1.5	1.5	3.25	0.74	75	17.8	64	14.4
1.5	2.5	4.75	1.23	74	18.0	66	24.3
1.0	1.0	2.78	0.49	79	0	0	3.3
1.5	1.0	2.50	0.49	77	11.1	32	9.5
2.0	1.0	2.28	0.46	79	26.4	94	18.7
2.5	1.0	2.11	0.42	80	36.2	156	30.8

It is interesting to find that CAH ($\Delta\theta$) does not alter monotonically with θ_Y as shown in Table II. On lyophobic rough surfaces ($\theta_Y > 90^\circ$), both $\Delta\theta$ and f_c decrease with increasing θ_Y. Their changes are in accordance with the extent of impregnation. As $\theta_Y = 127^\circ$, the nanodrop is able to exhibit the random motion in the absence of external forces. Therefore, one has $f_c = 0$ and $\Delta\theta \approx 0$. Based on the extent of impregnation, the nanodrop can be regarded in the Cassie-Baxter state. This consequence is consistent with the concept of superhydrophobic surfaces where most of the drop base is in contact with the air pockets. Hence, CAH is essentially absent. On lyophilic surfaces ($\theta_Y < 90^\circ$), one expects that $\Delta\theta$ increases with the growth of wettability corresponding to the extent of impregnation. However, it is found that $\Delta\theta$ and f_c decline significantly as θ_Y descends. From the viewpoint of impregnation, the drop is essentially in the Wenzel state. However, the grooves near the edge of the drop is not fully impregnated but susceptible to imbibe liquid (Ref. [44], Movie S1). This condition is getting serious as θ_Y is decreased. Therefore, a smaller f_c is able to move the drop forward but a small portion of liquid is always left in the grooves. As $\theta_Y = 63^\circ$, one has f_c approaching zero and $\Delta\theta$ is difficult to determine. The above simulation results reveal that for a specified roughness, the maximum extent of CAH tends to occur at surfaces with the wettability away from being highly lyophobic and lyophilic.

D. Effect of roughness on the most stable CA and CAH

In addition to the wettability of liquid on solid surface, it is known that the most stable CA and CAH depend significantly on surface roughness. The influences of roughness on θ'_Y and $\Delta\theta$ can be investigated if the structure of regular grooves is systematically varied for a specified wettability. For surfaces with $\theta_Y = 85^\circ$, the simulation outcomes are listed in Table III for various values of groove width W and height H. Here all grooves are rectangular $L = W$ and the distance between two adjacent grooves is $G = 0.5$.

As H is increased from 0.5 to 2.5, the area ratio (r) and arithmetic average of the 3D roughness (S_a) are increased but the area fraction (α) remains unchanged, 0.44. It is found that θ'_Y declines with increasing H. This result is consistent with the Wenzel model. Since the groove size is slightly greater than the size of a DPD bead, the effect of the groove surface on the extent of impregnation is significant. In this case, the

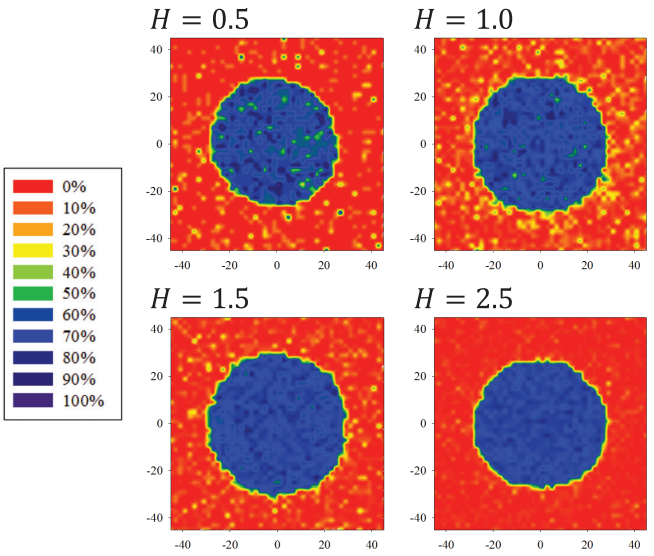

FIG. 7. The contour plot of the liquid density in the groove compared to that in the bulk for various groove depths H.

liquid density in the groove is about 70% of that in the bulk (Fig. 7). The underestimation of θ'_Y by the Wenzel model may be explained by the smaller value of r (effective area ratio). As H is increased, both $\Delta\theta$ and f_c grow. Nonetheless, CAH becomes insensitive to H (or S_a) for $H \geqslant 1.5$. For shallow grooves ($H \leqslant 1.0$), impregnated liquid in the roughness is carried away by a moving drop ($f > f_c$) (Ref. [44], Movie S2). In contrast, for deep grooves, liquid trapped in the roughness is left behind by a sliding drop (Ref. [44], Movie S3). That is, the external force overcomes the liquid-liquid cohesive force and the breakup of the nanodrop is resulted. As the breakup mechanism dominates, CAH is independent of the groove height.

As W is increased from 1.0 to 2.5, the area ratio (r) and arithmetic average of the 3D roughness (S_a) decline and the

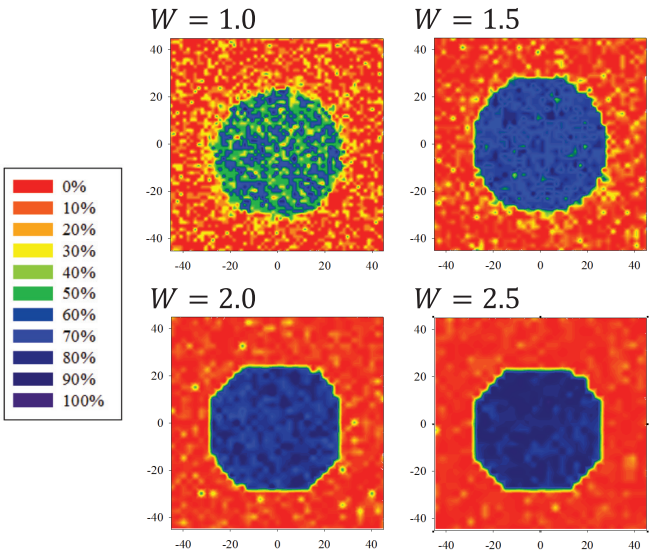

FIG. 8. The contour plot of the liquid density in the groove compared to that in the bulk for various groove widths W. As W is increased, the contact line gradually becomes noncircular.

area fraction (α) is reduced from 0.56 to 0.31. However, the liquid density in the groove grows from 55% to 82% of that in the bulk (Fig. 8). As depicted in Table III, it seems that θ_Y' is not sensitive to W. This consequence does not agree with the Wenzel model. The failure may be attributed to the opposite trend of the extent of impregnation realized from the area ratio and the liquid density in the groove. In contrast to θ_Y', it is found that both $\Delta\theta$ and f_c grow with increasing W. As $W = 1.0$, the random motion of the drop is clearly seen. Therefore, $f_c = 0$ is observed and CAH on such a surface is absent. However, as $W = 2.5$, the nanodrop is strongly pinned by the grooves. For $f = f_c$, one has $\theta_a \approx 104^\circ$ and $\theta_r \approx 68^\circ$. This result indicates that CAH is serious because $\Delta\theta > 30^\circ$. It is worth mentioning that as W is increased, the contact line gradually becomes noncircular due to the edge effect of the grooves [45], as shown in Fig. 8. According to our simulation results, serious CAH on a patterned rough surface results mainly from the large mouth of grooves instead of the depth or S_a.

IV. CONCLUSIONS

The wetting behavior of nanodrops on smooth or patterned rough surfaces are investigated by MDPD. On a smooth surface, a nanodrop exhibits different θ_Y via varying the attractive parameter between liquid and solid and Young's equation is valid. Moreover, nanodrops show the random motion due to thermal fluctuations, indicating the absence of CAH. The diffusivity decays as θ_Y is decreased. By the spontaneous partial wetting of a spherical drop on a rough surface, the equilibrium CA θ_Y' is different from θ_Y and corresponds to the most stable CA. The contact line of a nanodrop is pinned by grooves and CAH appears. For a specified patterned roughness, the extent of CAH is determined by increasing and decreasing the drop volume or exerting a horizontal external force f. The typical hysteresis loops of the apparent CA and base diameter of the drop are acquired. Both approaches yield consistent results and can be employed to explore CAH in simulations.

θ_Y is varied to examine the effect of wettability on the most stable CA and CAH for a patterned rough surface. θ_Y' grows as θ_Y is increased. However, θ_Y' deviates from the theoretical value predicted by the Wenzel or Cassie-Baxter models. This outcome is explained by the extent of impregnation, which varies with the groove position and wettability. The liquid density in the groove is always smaller than that in the bulk. Interestingly, CAH changes nonmonotonically with θ_Y for a specified roughness. The maximum $\Delta\theta$ tends to occur at surfaces with medium wettability ($\theta_Y \sim 90^\circ$). As a surface becomes more lyophilic, the grooves outside the drop edge becomes susceptible to imbibe liquid and CAH tends to vanish. In addition, the groove structure is systematically varied to examine the effect of roughness on θ_Y' and $\Delta\theta$. As the groove depth is increased, CAH rises but becomes unchanged eventually. In contrast, as the groove width is increased, θ_Y' does not change but CAH grows significantly. Our simulation results reveal that CAH depends more on the groove width than the depth.

ACKNOWLEDGMENT

Y.-J.S. and H.-K.T. thank the Ministry of Science and Technology of Taiwan for financial support.

[1] J. Zhang and Y. Han, A topography/chemical composition gradient polystyrene surface: Toward the investigation of the relationship between surface wettability and surface structure and chemical composition, Langmuir **24**, 796 (2008).

[2] Y. Ito, M Heydari, A. Hashimoto, T. Konno, A. Hirasawa, S. Hori, K. Kurita, and A. Nakajima, The movement of a water droplet on a gradient surface prepared by photodegradation, Langmuir **23**, 1845 (2007).

[3] P. G. de Gennes, F. Brochard-Wyart, and D. Quéré, *Capillarity and Wetting Phenomena, Drops, Bubbles, Pearls, Waves* (Springer, New York, 2004).

[4] L. Feng, Y. Zhang, Y. Cao, X. Yea, and L. Jiang, The effect of surface microstructures and surface compositions on the wettabilities of flower petals, Soft Matter **7**, 2977 (2011).

[5] D. Öner and T. J. McCarthy, Ultrahydrophobic surfaces. Effects of topography length scales on wettability, Langmuir **16**, 7777 (2000).

[6] R. E. Johnson and R. H. Dettre, Contact angle hysteresis I. Study of an idealized rough surface, Adv. Chem. Ser. **43**, 112 (1964).

[7] A. Marmur, Wetting on hydrophobic rough surfaces: To be heterogeneous or not to be? Langmuir **19**, 8343 (2003).

[8] C. W. Extrand, Contact angles and hysteresis on surfaces with chemically heterogeneous islands, Langmuir **19**, 3793 (2003).

[9] S.-J. Hong, C.-C. Chang, T.-H. Chou, Y.-J. Sheng, and H.-K. Tsao, A drop pinned by a designed patch on a tilted superhydrophobic surface: Mimicking desert beetle, J. Phys. Chem. C **116**, 26487 (2012).

[10] J. N. Israelachvili, *Intermolecular and Surface Forces* (Academic Press, New York, 1985).

[11] T.-H. Chou, S.-J. Hong, Y.-J. Sheng, and H.-K. Tsao, Drops sitting on a tilted plate: Receding and advancing pinning, Langmuir **28**, 5158 (2012).

[12] S.-J. Hong, F.-M. Chang, T.-H. Chou, S. H. Chan, Y.-J. Sheng, and H.-K. Tsao, Anomalous contact angle hysteresis of a captive bubble: Advancing contact line pinning, Langmuir **27**, 6890 (2011).

[13] N. T. Chamakos, M. E. Kavousanakis, and A. G. Papathanasiou, Enabling efficient energy barrier computations of wetting transitions on geometrically patterned surfaces, Soft Matter **9**, 9624 (2013).

[14] A. Promraksa and L.-J. Chen, Modeling contact angle hysteresis of a liquid droplet sitting on a cosine wave-like pattern surface, J. Colloid Interface Sci. **384**, 172 (2012).

[15] C.-C. Chang, C.-J. Wu, Y.-J. Sheng, and H.-K. Tsao, Air pocket stability and the imbibition pathway in droplet wetting, Soft Matter **11**, 7308 (2015).

[16] J. F. Joanny and P. G. de Gennes, A model for contact angle hysteresis, J. Chem. Phys. **81**, 552 (1984).

[17] N. Miljkovic, R. Enright, Y. Nam, K. Lopez, N. Dou, J. Sack, and E. N. Wang, Jumping-droplet-enhanced condensation on

scalable superhydrophobic nanostructured surfaces, Nano Lett. **13**, 179 (2013).
[18] E. Bormashenko, T. Stein, G. Whyman, Y. Bormashenko, and R. Pogreb, Wetting properties of the multiscaled nanostructured polymer and metallic superhydrophobic surfaces, Langmuir **22**, 9982 (2006).
[19] Y. C. Jung and B. Bhushan, Wetting transition of water droplets on superhydrophobic patterned surfaces, Scr. Mater. **57**, 1057 (2007).
[20] T. Deng, K. K. Varanasi, M. Hsu, N. Bhate, C. Keimel, J. Stein, and M. Blohm, Nonwetting of impinging droplets on textured surfaces, Appl. Phys. Lett. **94**, 133109 (2009).
[21] Y. C. Jung and B. Bhushan, Wetting behavior of water and oil droplets in three-phase interfaces for hydrophobicity/philicity and oleophobicity/philicity, Langmuir **25**, 14165 (2009).
[22] F.-C. Wang and Y.-P. Zhao, Contact angle hysteresis at the nanoscale: A molecular dynamics simulation study, Colloid Polym. Sci. **291**, 307 (2013).
[23] B. Kong and X. Yang, Dissipative particle dynamics simulation of contact angle hysteresis on a patterned solid/air composite surface, Langmuir **22**, 2065 (2006).
[24] C. Yang, U. Tartaglino, and B. N. J. Persson, Nanodroplets on rough hydrophilic and hydrophobic surfaces, Eur. Phys. J. E **25**, 139 (2008).
[25] Y. Wang and S. Chen, Numerical study on droplet sliding across micropillars, Langmuir **31**, 4673 (2015).
[26] G. O. Berim and E. Ruckenstein, Nanodrop on a nanorough hydrophilic solid surface: Contact angle dependence on the size, arrangement, and composition of the pillars, J. Colloid Interface Sci. **359**, 304 (2011).
[27] A. Malijevský, Does surface roughness amplify wetting? J. Chem. Phys. **141**, 184703 (2014).
[28] A. P. Malanoski, B. J. Johnson, and J. S. Erickson, Contact angles on surfaces using mean field theory: Nanodroplets vs. nanoroughness, Nanoscale **6**, 5260 (2014).
[29] G. O. Berim and E. Ruckenstein, Nanodrop on a smooth solid surface with hidden roughness. Density functional theory considerations, Nanoscale **7**, 7873 (2015).
[30] A. J. Briant, A. J. Wagner, and J. M. Yeomans, Lattice Boltzmann simulations of contact line motion. I. Liquid-gas systems, Phys. Rev. E **69**, 031602 (2004).
[31] R. Ledesma-Aguilar, D. Vella, and J. M. Yeomans, Lattice-Boltzmann simulations of droplet evaporation, Soft Matter **10**, 8267 (2014).
[32] L. Moevius, Y. Liu, Z. Wang, and J. M. Yeomans, Pancake bouncing: simulations and theory and experimental verification, Langmuir **30**, 13021 (2014).
[33] Y. Liu, J. Wang, and X. Zhang, Accurate determination of the vapor-liquid-solid contact line tension and the viability of Young equation, Sci. Rep. **3**, 2008 (2013).
[34] C. D. Daub, J. Wang, S. Kudesia, D. Bratko, and A. Luzar, The influence of molecular-scale roughness on the surface spreading of an aqueous nanodrop, Faraday Discuss. **146**, 67 (2010).
[35] F. Leroy and F. Müller-Plathe, Rationalization of the behavior of solid-liquid surface free energy of water in Cassie and Wenzel wetting states on rugged solid surfaces at the nanometer scale, Langmuir **27**, 637 (2011).
[36] P. B. Warren, Vapor-liquid coexistence in many-body dissipative particle dynamics, Phys. Rev. E **68**, 066702 (2003).
[37] Z. Wang, H.-Y. Chen, Y.-J. Sheng, and H.-K. Tsao, Diffusion, sedimentation equilibrium, and harmonic trapping of run-and-tumble nanoswimmers, Soft Matter **10**, 3209 (2014).
[38] H.-L. Wu, P.-Y. Chen, C.-L. Chi, H.-K. Tsao, and Y.-J. Sheng, Vesicle deposition on hydrophilic solid surfaces, Soft Matter **9**, 1908 (2013).
[39] J. H. Irving and J. G. Kirkwood, The statistical mechanical theory of transport processes. IV. The equations of hydrodynamics, J. Chem. Phys. **18**, 817 (1950).
[40] A. Ghoufi and P. Malfreyt, Calculation of the surface tension from multibody dissipative particle dynamics and Monte Carlo methods, Phys. Rev. E **82**, 016706 (2010).
[41] F. J. Montes Ruiz-Cabello, M. A. Rodríguez-Valverde, and M. A. Cabrerizo-Vílchez, A new method for evaluating the most stable contact angle using tilting plate experiments, Soft Matter **7**, 10457 (2011).
[42] J. A. White, M. J. Santos, M. A. Rodríguez-Valverde, and S. Velasco, Numerical study of the most stable contact angle of drops on tilted surfaces, Langmuir **31**, 5326 (2015).
[43] F. J. Montes Ruiz-Cabello, M. A. Rodríguez-Valverde, and M. A. Cabrerizo-Vílchez, Equilibrium contact angle or the most-stable contact angle? Adv. Colloid Interface Sci. **206**, 320 (2014).
[44] See Supplemental Material at http://link.aps.org/supplemental/10.1103/PhysRevE.94.042807 for movies S1, S2, and S3 demonstrating simulation results of nanodrops on various patterned rough surfaces.
[45] F.-M. Chang, S.-J. Hong, Y.-J. Sheng, and H.-K. Tsao, Wetting invasion and retreat across a corner boundary, J. Phys. Chem. C **114**, 1615 (2010).